

Scalable learning of macroscopic stochastic dynamics

Mengyi Chen¹, Pengru Huang², Kostya S. Novoselov^{2, 3}, and Qianxiao Li^{1, 2, *}

¹Department of Mathematics, National University of Singapore, Singapore, Singapore

²Institute for Functional Intelligent Materials, National University of Singapore, Singapore, Singapore

³Materials Science and Engineering, National University of Singapore, Singapore, Singapore

*Corresponding authors: qianxiao@nus.edu.sg

Abstract

Macroscopic dynamical descriptions of complex physical systems are crucial for understanding and controlling material behavior. With the growing availability of data and compute, machine learning has become a promising alternative to first-principles methods to build accurate macroscopic models from microscopic trajectory simulations. However, for spatially extended systems, direct simulations of sufficiently large microscopic systems that inform macroscopic behavior is prohibitive. In this work, we propose a framework that learns the macroscopic dynamics of large stochastic microscopic systems using only small-system simulations. Our framework employs a partial evolution scheme to generate training data pairs by evolving large-system snapshots within local patches. We subsequently identify the closure variables associated with the macroscopic observables and learn the macroscopic dynamics using a custom loss. Furthermore, we introduce a hierarchical upsampling scheme that enables efficient generation of large-system snapshots from small-system trajectory distributions. We empirically demonstrate the accuracy and robustness of our framework through a variety of stochastic spatially extended systems, including those described by stochastic partial differential equations, idealised lattice spin systems, and a more realistic NbMoTa alloy system.

1 Introduction

Macroscopic observables characterize the collective behavior of complex microscopic dynamics and play a crucial role in real-world applications. They are typically functions of the full microscopic system. For example, magnetization is defined as the average of the local magnetic moments, and temperature as the average kinetic energy per degree of freedom. For alloy systems, macroscopic observables such as thermal conductivity, electrical conductivity, and magnetization are governed by a variety of microscopic interactions, including collective electron scattering mechanisms, lattice vibrations, and microscopic spin coupling interactions [1]. These macroscopic observables capture the material's overall behavior and functionality.

To obtain accurate time evolution of macroscopic observables, large-scale microscopic simulations over extended times are often required, yet their high computational expense remains the main bottleneck [2–4]. For example, Density Functional Theory (DFT) and the related *Ab Initio* Molecular Dynamics (AIMD) represent a milestone in computational methods for studying molecules and solid-state materials at the quantum mechanical level. However, due to the well-known exponential wall challenge, where computational expense increases rapidly with the number of particles, DFT simulations are usually limited to relatively small systems that may be insufficient in capturing true macroscopic behavior [5, 6].

Various approaches have been developed to overcome the computational bottleneck. The Kinetic Monte Carlo (KMC) algorithm represents the microscopic dynamics as a Markov chain by coarse-graining the time axis [7–9]. The transition rates for all possible events need to be computed for every KMC step. Therefore, KMC is still computationally prohibitive for large systems [10, 11]. Machine learning force fields (MLFFs) replace the

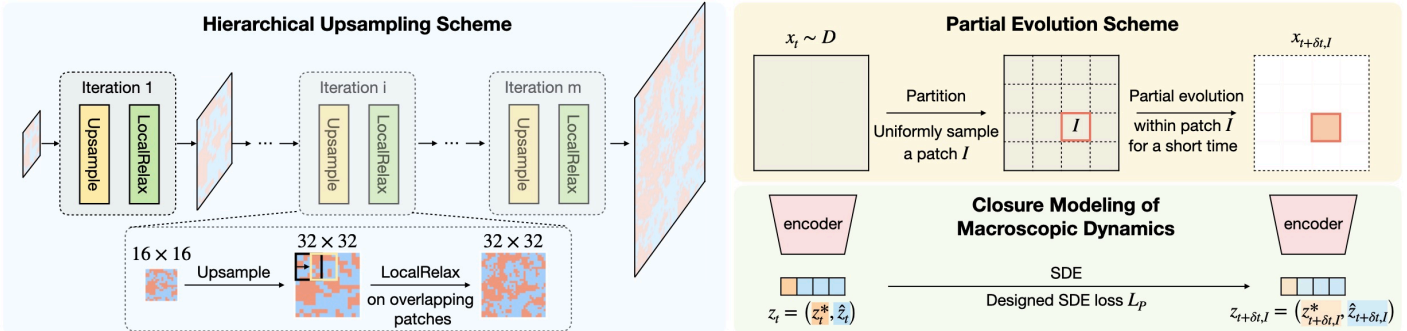


Figure 1: Schematic illustration of our framework. The hierarchical upsampling scheme generates the large-system distribution \mathcal{D} from the small-system trajectory distribution \mathcal{D}_s through multiple iterations, each consisting of an UPSAMPLE and a LOCALRELAX step. An example of one iteration for the Ising model is shown. For the partial evolution scheme, for every $\mathbf{x}_t \sim \mathcal{D}$, a patch \mathcal{I} is first uniformly sampled, then the microscopic dynamics is evolved locally within the patch \mathcal{I} for a short time to yield $\mathbf{x}_{t+\delta t, \mathcal{I}}$. For the closure modeling, an autoencoder is trained to discover the closure variables to the macroscopic observables, and the macroscopic dynamics are identified with the designed loss \mathcal{L}_p .

expensive *ab initio* force computations with efficient neural network-based predictions [12–15]. When applying MLFFs to molecular dynamics simulations, the time step of the molecular dynamics simulation must be chosen on the scale of femtoseconds to capture atomic vibrations. Consequently, millions to billions of integration steps are required for the simulation, and atomic forces are computed for each time step, still resulting in high computational cost for large systems [16]. Coarse-grained MLFFs further improve computational efficiency by mapping several atoms onto effective particles, thereby reducing the number of degrees of freedom. However, the training of coarse-grained MLFFs requires microscopic simulation data, and the largest barrier to applying coarse-grained MLFFs to large systems is generating enough training data [17–21]. The closure modeling methods, instead, model the dynamics of macroscopic observables directly, but still rely on short microscopic simulations of the large system or microscopic forces on all atoms for macroscopic dynamics identification of large systems [22].

Despite their methodological differences, existing approaches all rely either on direct microscopic simulations or on training data derived from such simulations. However, due to the computational constraint, microscopic simulation for large systems with millions to billions of atoms over extended time is generally intractable. This leads to a natural question: Can accurate macroscopic dynamics of large systems be obtained when only small-system microscopic simulations are accessible? Chen and Li [23] proposed a training procedure on the microscopic coordinates that addresses this question for deterministic dynamics. However, their method requires partial computation of microscopic forces for the macroscopic dynamics identification. In the case of stochastic systems, where the dynamics are described by the conditional distribution of the next configuration given the current one, such microscopic forces are generally not well-defined. Hence, their method cannot be easily generalized to stochastic systems. Yet, stochastic microscopic systems are arguably more prevalent, especially in the modeling of chemical reactions, molecular dynamics, and ferromagnetic phase transitions [24]. The main goal of our method is to address the above question for stochastic dynamical systems.

In this work, we develop a framework that can accurately identify the macroscopic dynamics of stochastic microscopic systems, while requiring only microscopic simulations of small systems. Specifically, given the data distribution \mathcal{D} , composed of snapshots of large systems spanning states from far-from-equilibrium to near-equilibrium, we introduce a partial evolution scheme which evolves $\mathbf{x}_t \sim \mathcal{D}$ locally within a local patch \mathcal{I} for a short time δt to produce training data pairs $\{\mathbf{x}_t, \mathbf{x}_{t+\delta t, \mathcal{I}}\}$. Next, building on the workflow of Ref. [22], we identify the closure variables to the macroscopic observables and model the resulting dynamics via stochastic

differential equations (SDE). To adapt to the training data generated through the partial evolution scheme, we introduce a modified SDE loss and provide a theoretical justification. In addition, we design a hierarchical upsampling scheme that efficiently generates \mathcal{D} from the small-system trajectory distribution \mathcal{D}_s .

The key idea of our framework is summarized in Fig. 1. We provide a detailed description of each component in Section 2. We further validate the accuracy and robustness of our method through a variety of stochastic microscopic systems, including stochastic partial differential equations (SPDE) systems, spin systems, and a more realistic NbMoTa alloy system in Section 3.

2 METHODOLOGY

We focus on microscopic systems that are spatially extended, including SPDE systems, the Ising model, and alloy systems. We assume the microscopic time evolution can be modeled as a Markov process of a random variable supported on a finite but large lattice structure. Let the microscopic state be $\mathbf{x} = (\mathbf{x}_1, \dots, \mathbf{x}_n) \in \mathbb{R}^n$, where n represents the number of lattice sites of the system. We assume the lattice sites are arranged on a regular lattice structure, and \mathbf{x}_i represents some physical quantity associated with the i -th lattice site. To better illustrate this, we provide several examples. In SPDE systems, \mathbf{x} can be the state variables after spatial discretization on a regular grid, with n denoting the total number of grid points. In the Ising model, n denotes the number of spins, and $\mathbf{x}_i \in \{-1, 1\}$ represents the spin state of the i -th spin. The spins are arranged on a square lattice. In alloy systems, n denotes the number of atoms and \mathbf{x}_i represents the atom type of the i -th lattice site. The atoms are arranged on a regular lattice structure, depending on the crystal structure of the alloy, such as body-centered cubic (BCC), face-centered cubic (FCC), hexagonal close-packed (HCP), or diamond cubic.

In many real applications, we are interested in the dynamics of some macroscopic observables, denoted by $\mathbf{z}^* = \varphi^*(\mathbf{x})$. The form of φ^* is given beforehand, and φ^* can be applied to different system sizes. Since the underlying microscopic system is spatially extended, we are interested in the intensity quantities that do not scale with system size. For instance, in the Ising model, it is common to study the average magnetization $M = \sum_{i=1}^n \mathbf{x}_i/n$ instead of the total magnetization. In what follows, we will limit our discussion of macroscopic observables to intensity quantities.

Assume we are given a microscopic simulator \mathcal{S}_{n_s} , which can accurately simulate the microscopic dynamics of a small system up to size $n_s \ll n$ due to computational constraints. From this simulator, we obtain the trajectory distribution \mathcal{D}_s of the small system. The goal of this work is to identify the macroscopic dynamics of a large system of size n using only such small-scale simulations.

2.1 Closure modeling of macroscopic dynamics

Existing works on macroscopic dynamics identification typically involve two components: discovering the closures for macroscopic observables, and jointly identifying their dynamics [22, 25, 26]. Our work adopts the same two components for macroscopic dynamics identification. Assume we are given the data distribution \mathcal{D} of the large system, consisting of multiple snapshots of the large system, we will first generate temporal training data pairs as follows.

Partial evolution scheme. We partition the underlying regular lattice into $K = n/n_s$ small patches, each containing n_s lattice sites. For example, for the two-dimensional Ising model on a 64^2 square lattice, we partition the large square into 64 square patches of size $n_s = 8^2$. Let the index set of lattice sites in the k -th patch be \mathcal{I}^k , which is a subset of $\{1, \dots, n\}$ and contains n_s lattice sites. The state of the lattice sites in patch \mathcal{I}^k is then written as $\mathbf{x}_{\mathcal{I}^k} = \{\mathbf{x}_i\}_{i \in \mathcal{I}^k}$, and the microscopic state as $\mathbf{x} = (\mathbf{x}_{\mathcal{I}^1}, \dots, \mathbf{x}_{\mathcal{I}^K})$.

For each configuration $\mathbf{x}_t \sim \mathcal{D}$, we uniformly sample a patch \mathcal{I} from the K patches with probability $1/K$. Next, the microscopic simulator \mathcal{S}_{n_s} is used to evolve \mathbf{x}_t within the selected patch \mathcal{I} for a short time δt , yielding

the updated state $\mathbf{x}_{t+\delta t, \mathcal{I}}$. Consequently, the resulting training data pair is $\{\mathbf{x}_t, \mathbf{x}_{t+\delta t, \mathcal{I}}\}$. Note that the time step δt may also be random. For instance, δt is sampled from an exponential distribution in the case of kinetic Monte Carlo dynamics.

We will demonstrate how to identify the macroscopic dynamics from the training data pairs obtained from the partial evolution scheme.

Autoencoder for discovering closure variables. We employ an autoencoder architecture to discover closure variables $\hat{\mathbf{z}}$ associated with the macroscopic observables \mathbf{z}^* . The closure variables will capture the unresolved information by \mathbf{z}^* , and ensure the dynamics of $\mathbf{z} = (\mathbf{z}^*, \hat{\mathbf{z}})$ depend only on itself. For example, in our experiments, the dynamics of the Curie-Weiss model can be fully described by the magnetization, hence no closure variables will be needed if \mathbf{z}^* represents the magnetization. In contrast, for the Ising model, the magnetization alone cannot capture all the dynamical information, and additional closure variables are required so that the dynamics of \mathbf{z} only depend on itself.

Since the training data pairs take the form of $\{\mathbf{x}_t, \mathbf{x}_{t+\delta t, \mathcal{I}}\}$, We want the closure function to be well-defined for both the microscopic state \mathbf{x} and the microscopic state $\mathbf{x}_{\mathcal{I}}$, which are of different dimensions. Denote the closure function by $\hat{\varphi}$. To achieve this, $\hat{\varphi}$ is directly applied to $\mathbf{x}_{\mathcal{I}}$, yielding $\hat{\varphi}(\mathbf{x}_{\mathcal{I}})$. The closure representation for the full state \mathbf{x} is defined as the average of $\hat{\varphi}(\mathbf{x}_{\mathcal{I}})$ over all the patches:

$$\hat{\varphi}(\mathbf{x}) = \frac{1}{K} \sum_{\mathcal{I} \in \{\mathcal{I}^1, \dots, \mathcal{I}^K\}} \hat{\varphi}(\mathbf{x}_{\mathcal{I}}). \quad (1)$$

We denote the closure variables by $\hat{\mathbf{z}} = \hat{\varphi}(\mathbf{x})$, and concatenate it with the macroscopic observable $\mathbf{z}^* = \varphi^*(\mathbf{x})$ to form the full latent state $\mathbf{z} = (\mathbf{z}^*, \hat{\mathbf{z}}) = (\varphi^*(\mathbf{z}), \hat{\varphi}(\mathbf{x}))$. By definition of the closure variables, $\hat{\mathbf{z}}$ are intensive quantities, just like the macroscopic observables \mathbf{z}^* . Therefore, \mathbf{z} represents intensity quantities. Denote the encoder by $\varphi = (\varphi^*, \hat{\varphi})$ and the decoder by ψ , where φ^* is the predefined macroscopic observable function with no trainable parameters. The functions $\hat{\varphi}$ and ψ are parameterized by neural networks and are trained jointly. We omit the explicit dependence on the parameters for notational simplicity. The autoencoder is trained by minimizing the reconstruction loss:

$$\mathcal{L}_{\text{recon}} = \mathbb{E}_{\mathbf{x}_t} \|\psi \circ \varphi(\mathbf{x}_t) - \mathbf{x}_t\|_2^2. \quad (2)$$

Once the autoencoder is trained, we will generate the latent training data pair $\{\mathbf{z}_t, \mathbf{z}_{t+\delta t, \mathcal{I}}\}$ for the macroscopic dynamics identification:

$$\begin{aligned} \mathbf{z}_t &= \varphi(\mathbf{x}_t), \\ \mathbf{z}_{t+\delta t, \mathcal{I}} &:= \mathbf{z}_t + (\varphi(\mathbf{x}_{t+\delta t, \mathcal{I}}) - \varphi(\mathbf{x}_{t, \mathcal{I}})), \end{aligned} \quad (3)$$

where $\mathbf{x}_{t, \mathcal{I}}$ denotes the restriction of \mathbf{x}_t to the local patch \mathcal{I} . Next, we introduce the process of identifying macroscopic dynamics.

Macroscopic dynamics identification We model the Macroscopic dynamics with SDE:

$$d\mathbf{z}_t = \boldsymbol{\mu}(\mathbf{z}_t)dt + \boldsymbol{\Sigma}^{1/2}(\mathbf{z}_t)d\mathbf{B}_t, \quad (4)$$

where $\boldsymbol{\mu}$ is the drift term and $\boldsymbol{\Sigma}$ is the diffusion term. In most experiments, we adopt fully connected networks for both $\boldsymbol{\mu}$ and $\boldsymbol{\Sigma}$. For the NbMoTa alloy experiment in Section 3.4, we adopt OnsagerNet [22, 27] for $\boldsymbol{\mu}$ to account for more complex macroscopic dynamics. The OnsagerNet can capture physically interpretable and stable macroscopic dynamics by incorporating the generalized Onsager principle into the model structure, and its form is given by:

$$\boldsymbol{\mu}(\mathbf{z}_t) = -(\mathbf{M}(\mathbf{z}_t) + \mathbf{W}(\mathbf{z}_t))\nabla V(\mathbf{z}_t) + \mathbf{f}(\mathbf{z}_t), \quad (5)$$

where \mathbf{M} is a symmetric positive semi-definite matrix describing energy dissipation, \mathbf{W} is a skew-symmetric matrix describing energy conservation, V is a potential function, and \mathbf{f} is a vector field representing external forces.

Existing works train the SDE by minimize the negative log-likelihood [22, 28–30]:

$$\mathcal{L}[\boldsymbol{\mu}, \boldsymbol{\Sigma}] = \mathbb{E}_{\mathbf{z}_t, \mathbf{z}_{t+\delta t}} [-2 \log p(\mathbf{z}_{t+\delta t} | \mathbf{z}_t + \boldsymbol{\mu}(\mathbf{z}_t)\delta t, \boldsymbol{\Sigma}(\mathbf{z}_t)\delta t)], \quad (6)$$

where $\mathbf{z}_{t+\delta t}$ denotes the latent state obtained by evolving the full system from \mathbf{z}_t over a time step δt . The conditional distribution p is given by the Gaussian distribution $\mathcal{N}(\mathbf{z}_{t+\delta t}; \mathbf{z}_t + \boldsymbol{\mu}(\mathbf{z}_t)\delta t, \boldsymbol{\Sigma}(\mathbf{z}_t)\delta t)$, obtained by discretizing the SDE with the Euler-Maruyama scheme.

In our setting, however, $\mathbf{z}_{t+\delta t, \mathcal{I}}$ is not obtained by evolving the full system by δt . Instead, it results from a partial evolution over a localized spatial patch. To account for this, we adapt the SDE loss as follows:

$$\mathcal{L}_p[\boldsymbol{\mu}, \boldsymbol{\Sigma}] = \mathbb{E}_{\mathbf{z}_t, \mathbf{z}_{t+\delta t, \mathcal{I}}} [-2 \log p(\mathbf{z}_{t+\delta t, \mathcal{I}} | \mathbf{z}_t + \boldsymbol{\mu}(\mathbf{z}_t)\delta t, \mathbf{K}\boldsymbol{\Sigma}(\mathbf{z}_t)\delta t)]. \quad (7)$$

The only difference between \mathcal{L} and \mathcal{L}_p is that we multiply a coefficient K to the diffusion term in \mathcal{L}_p . We can interpret the influence of K qualitatively. Since $K > 1$ scales the diffusion term, K will reduce the magnitude of the diffusion term. During the data generation of $\mathbf{x}_{t+\delta t, \mathcal{I}}$ from \mathbf{x}_t , we introduce additional randomness by performing partial evolution. Therefore, in the identification of macroscopic dynamics, we multiply the diffusion term by K to correct for the extra stochasticity.

To learn the macroscopic dynamics, we parametrize both $\boldsymbol{\mu}$ and $\boldsymbol{\Sigma}$ with neural networks, denoted by $\boldsymbol{\mu}_\theta$ and $\boldsymbol{\Sigma}_\theta$, respectively. The training objective is given by the loss function:

$$\mathcal{L}_p(\boldsymbol{\theta}) := \mathcal{L}_p[\boldsymbol{\mu}_\theta, \boldsymbol{\Sigma}_\theta]. \quad (8)$$

We minimize $\mathcal{L}_p(\boldsymbol{\theta})$ to obtain the optimal parameter.

It is important to observe that in Eq. (3), we define $\mathbf{z}_{t+\delta t, \mathcal{I}}$ in a nontrivial way, while the most naive way will be $\mathbf{z}_{t+\delta t, \mathcal{I}} = \varphi(\mathbf{x}_{t+\delta t, \mathcal{I}})$. Note that the loss function $\mathcal{L}_p(\boldsymbol{\theta})$ involves the weighted norm of the residual $\mathbf{z}_{t+\delta t, \mathcal{I}} - \mathbf{z}_t - \boldsymbol{\mu}(\mathbf{z}_t)\delta t$ since p represents a gaussian distribution. If we define $\mathbf{z}_{t+\delta t, \mathcal{I}} = \varphi(\mathbf{x}_{t+\delta t, \mathcal{I}})$ in the naive way, we will have:

$$\mathbf{z}_{t+\delta t, \mathcal{I}} - \mathbf{z}_t = \frac{1}{K} \sum_{\mathcal{J}} (\varphi(\mathbf{x}_{t+\delta t, \mathcal{I}}) - \varphi(\mathbf{x}_{t, \mathcal{J}})), \quad (9)$$

which is the average of $\varphi(\mathbf{x}_{t+\delta t, \mathcal{I}}) - \varphi(\mathbf{x}_{t, \mathcal{J}})$. Since $\varphi(\mathbf{x}_{t+\delta t, \mathcal{I}})$ may be very different from $\varphi(\mathbf{x}_{t, \mathcal{J}})$ when $\mathcal{J} \neq \mathcal{I}$, the resulting $\mathbf{z}_{t+\delta t, \mathcal{I}} - \mathbf{z}_t$ will be very noisy. However, the definition in Eq. (3) will yield:

$$\mathbf{z}_{t+\delta t, \mathcal{I}} - \mathbf{z}_t = \varphi(\mathbf{x}_{t+\delta t, \mathcal{I}}) - \varphi(\mathbf{x}_{t, \mathcal{I}}), \quad (10)$$

which directly measures the change in the patch \mathcal{I} , thus reducing noise and leading to more stable training. We refer to the approach that adopts the naive formulation $\mathbf{z}_{t+\delta t, \mathcal{I}} = \varphi(\mathbf{x}_{t+\delta t, \mathcal{I}})$ and identifies the macroscopic dynamics via \mathcal{L} as the baseline. A detailed comparison of our method with the baseline is provided in Section 3.

Theoretical justification. In many microscopic systems, the microscopic interactions between lattice sites are local. For instance, microscopic interactions are limited to the first nearest neighbor in the Ising model, and are limited to a finite cutoff distance in alloy systems. Under such cases, when δt is small enough, the increments:

$$\begin{aligned} \mathbf{z}_{t+\delta t, \mathcal{I}} - \mathbf{z}_t &= \varphi(\mathbf{x}_{t+\delta t, \mathcal{I}}) - \varphi(\mathbf{x}_{t, \mathcal{I}}), \\ \mathbf{z}_{t+\delta t, \mathcal{J}} - \mathbf{z}_t &= \varphi(\mathbf{x}_{t+\delta t, \mathcal{J}}) - \varphi(\mathbf{x}_{t, \mathcal{J}}), \end{aligned} \quad (11)$$

can be approximately independent for disjoint patches $\mathcal{I} \neq \mathcal{J}$.

Let $\tilde{\mathbf{x}}_{t+\delta t, \mathcal{I}}$ be the microscopic state obtained by first evolving the full system from \mathbf{x}_t for time step δt , and subsequently restricted to the local patch \mathcal{I} . Under the local interaction assumption and for sufficiently small δt , the distribution of $\tilde{\mathbf{x}}_{t+\delta t, \mathcal{I}}$ can be well approximated by $\mathbf{x}_{t+\delta t, \mathcal{I}}$ obtained by partial evolution:

$$\tilde{\mathbf{x}}_{t+\delta t, \mathcal{I}} \stackrel{d}{\approx} \mathbf{x}_{t+\delta t, \mathcal{I}}, \quad \forall I \in \mathcal{I}. \quad (12)$$

Furthermore, since we consider a sufficiently large microscopic system and the macroscopic observables are intensive quantities, the macroscopic observable of the full system can be approximated by the average of the macroscopic observable on small patches:

$$\varphi^*(\mathbf{x}) \approx \frac{1}{K} \sum_{\mathcal{I}} \varphi^*(\mathbf{x}_{\mathcal{I}}). \quad (13)$$

Eq. (13) will hold exactly when the macroscopic observable can be expressed as the mean of a function that depends only on individual lattice sites, such as the magnetization. For more complex macroscopic observables, the equality is only approximate, but the approximation improves and becomes accurate in the limit of a large system size.

We provide a theoretical justification for the loss \mathcal{L}_p under the above conditions:

Theorem 1. *If $\mathbf{z}_{t+\delta t, \mathcal{I}} - \mathbf{z}_t$ is independent of $\mathbf{z}_{t+\delta t, \mathcal{J}} - \mathbf{z}_t$ when $\mathcal{I} \neq \mathcal{J}$, and if both Eq. (12) and Eq. (13) hold exactly:*

$$\begin{aligned} \mathbf{x}_{t+\delta t, \mathcal{I}} &\stackrel{d}{=} \tilde{\mathbf{x}}_{t+\delta t, \mathcal{I}}, \quad \forall I \in \mathcal{I}, \\ \varphi^*(\mathbf{x}) &= \frac{1}{K} \sum_{\mathcal{I}} \varphi^*(\mathbf{x}_{\mathcal{I}}). \end{aligned} \quad (14)$$

Then there exists a unique minimizer $(\boldsymbol{\mu}^, \boldsymbol{\Sigma}^*)$ of $\mathcal{L}[\boldsymbol{\mu}, \boldsymbol{\Sigma}]$, and a unique minimizer $(\boldsymbol{\mu}^\dagger, \boldsymbol{\Sigma}^\dagger)$ of $\mathcal{L}_p[\boldsymbol{\mu}, \boldsymbol{\Sigma}]$, such that:*

$$\boldsymbol{\mu}^* = \boldsymbol{\mu}^\dagger, \quad \boldsymbol{\Sigma}^* = \boldsymbol{\Sigma}^\dagger. \quad (15)$$

The proof is based on a direct computation of the first and second variations of the loss functions. We provide the full proof in Section B. Theorem 1 theoretically justifies our framework: Under appropriate conditions, the macroscopic dynamics learned from data generated via partial evolution are as accurate as those learned from full, computationally expensive microscopic simulations.

2.2 Hierarchical upsampling scheme

Algorithm 1 Hierarchical Upsampling Scheme

Require:

\mathcal{D}_s : trajectory distribution of small system
 N_{iter} : number of iterations
1: Initialize $\mathcal{D}^{(0)} \leftarrow \mathcal{D}_s$
2: **for** $i = 1$ **to** N_{iter} **do**
3: $\mathcal{D}^{(i)} \leftarrow \text{LOCALRELAX}(\text{UPSAMPLE}(\mathcal{D}^{(i-1)}))$
4: $\mathcal{D} \leftarrow \mathcal{D}^{(N_{\text{iter}})}$
5: **return** \mathcal{D} ▷ data distribution of the large system

In Section 2.1, we assume access to the data distribution \mathcal{D} , which contain multiple snapshots of large systems. In practice, however, direct access to \mathcal{D} is typically unavailable, as only microscopic simulations of small systems can be performed. To address this, We introduce a hierarchical upsampling scheme for generating the large-system data distribution \mathcal{D} from the small-system trajectory distribution \mathcal{D}_s . The hierarchical upsampling scheme is illustrated in Algorithm 1. It consists of multiple iterations, each involving two steps: UPSAMPLE and LOCALRELAX. In the UPSAMPLE step, the configurations in $\mathcal{D}^{(i)}$ are expanded into configurations of size m times larger, where $m \geq 2$ is an integer. Next, we apply a LOCALRELAX step to remove the unphysical artifacts that are introduced in the UPSAMPLE step. More specifically, each generated large-system configuration is

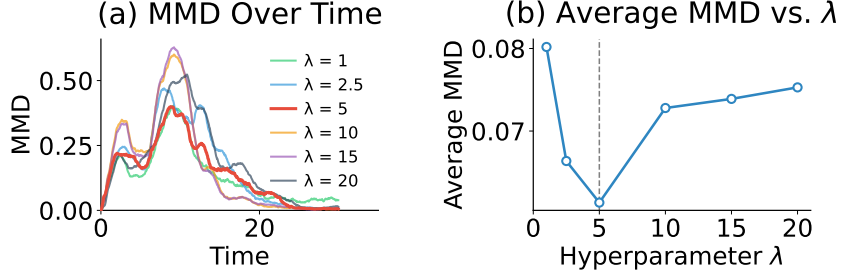


Figure 2: Results on the stochastic Predator-Prey system. (a) The MMD is plotted as a function of time. (b) The average MMD over the entire simulation time is reported as a function of the hyperparameter λ .

divided into overlapping patches of size n_s , and short-time relaxation or local dynamics evolution is applied within each patch.

For example, consider the two-dimensional Ising Model to be introduced in Section 3.3, where the microscopic dynamics is chosen to be the continuous-time Glauber dynamics. We assume direct simulations are feasible only for systems up to size $n_s = 8^2$. Starting from the small-system trajectory distribution \mathcal{D}_s , we apply the hierarchical upsampling scheme for $N_{\text{iter}} = 3$ iterations to obtain the large-system data distribution \mathcal{D} of size $n = 64^2$. In the first iteration, the UPSAMPLE step replicates each spin into a $m = 2^2$ block, yielding a 16^2 dimensional system. Next, we apply the LOCALRELAX step by dividing each 16^2 dimensional configuration into 16 patches of size $n_s = 8^2$ with a stride of 4. Within each patch, we run the continuous-time Glauber dynamics for a short time to remove the unphysical artifacts introduced in the UPSAMPLE step. In the second iteration, starting from the 16^2 dimensional data distribution $\mathcal{D}^{(1)}$, we repeat the UPSAMPLE and LOCALRELAX step to obtain $\mathcal{D}^{(2)}$ for the 32^2 dimensional system. Subsequently, in the third iteration, we obtain the target large-system distribution \mathcal{D} of size 64^2 from $\mathcal{D}^{(2)}$. We provide a graphical illustration of one iteration for the Ising model in Fig. 1 (a). The concrete form of UPSAMPLE and LOCALRELAX may vary for different microscopic systems, and further details are given in Section 3.

By generating training data through a hierarchical upsampling and partial evolution scheme, our method circumvents the expensive, large-system microscopic simulations that are required by most of the existing methods. The main computational savings of our method come from the efficient generation of training data.

3 RESULTS

In this section, we empirically validate the accuracy and robustness of our method across various microscopic systems. We first demonstrate our method on a SPDE system and spin systems, and then validate it on a more realistic NbMoTa alloy system.

3.1 Stochastic Predator-Prey system

We first consider a one-dimensional SPDE system, mainly to validate the correctness of our method and investigate the impact of the coefficient K in the designed loss \mathcal{L}_p . The stochastic Predator-Prey system is given by Eq. (16), where u, v denote the dimensionless populations of the prey and predator, and ξ_u, ξ_v are independent space-time white noise terms. In our experiment, we set the parameters $a = 3, b = 0.4, D = 0$ and

$$\sigma_u = \sigma_v = 0.02.$$

$$\begin{aligned} \frac{\partial u}{\partial t} &= u(1 - u - v) + D \frac{\partial^2 u}{\partial x^2} + \sigma_u \xi_u(t, x), \\ \frac{\partial v}{\partial t} &= av(u - b) + \frac{\partial^2 v}{\partial x^2} + \sigma_v \xi_v(t, x), \\ x \in \Omega &= [0, 1], \quad t \geq 0, \end{aligned} \tag{16}$$

We impose Neumann boundary conditions:

$$\frac{\partial u}{\partial x}(t, 0) = \frac{\partial u}{\partial x}(t, 1) = 0, \quad \frac{\partial v}{\partial x}(t, 0) = \frac{\partial v}{\partial x}(t, 1) = 0. \tag{17}$$

The initial conditions are defined as:

$$\begin{aligned} u(x, 0) &= c_1 + c_2 \cos(10\pi x), \\ v(x, 0) &= c_1 - c_2 \cos(10\pi x), \end{aligned} \tag{18}$$

where $c_1 \sim \mathcal{U}(0.05, 0.15)$, $c_2 \sim \mathcal{U}(0.45, 0.55)$.

For training data generation, we first generate the small-system distribution \mathcal{D}_s by discretizing the spatial domain Ω into 100 uniform grids. We then solve Eq. (16) from $t = 0$ to $T = 30$ with time step $\delta t = 0.01$. The small system thus contains $n_s = 100$ lattice sites. The goal is to learn the macroscopic observables of a large system discretized on $n = 200$ uniform grid points. To construct the large-system distribution \mathcal{D} , we perform an UPSAMPLE step by linearly interpolating the solution from the coarse grid with 100 points onto a finer grid with 200 points. Since this interpolation does not introduce unphysical artifacts, the LOCALRELAX step is not required here. The $n = 200$ uniform grids are partitioned into $K = 5$ patches, each containing 40 grids. For each $\mathbf{x}_t \sim \mathcal{D}$, we first uniformly sample a patch with $p = 1/5$, and subsequently evolve the system locally within the patch for one time step $\delta t = 0.01$ to obtain the updated state $\mathbf{x}_{t+\delta t, \mathcal{I}}$.

The macroscopic observable \mathbf{z}^* of interest is chosen to be the mean of the populations of the prey and predator over the spatial grid points, which is two-dimensional. We identify another 2 closure variables using an autoencoder, hence the dimension of \mathbf{z} is 4. The only difference between \mathcal{L} and \mathcal{L}_p lies in the coefficient multiplying the diffusion term. We treat the coefficient as a hyperparameter λ and train the SDE with different values of λ . Theoretical analysis in Theorem 1 shows that the optimal value of λ is K under appropriate conditions. We explore various values of λ to empirically investigate the influence of λ .

Fig. 2 shows the result on the 9 test datasets with different combinations of parameters $(c_1, c_2) \in \{0.05, 0.10, 0.15\} \times \{0.45, 0.50, 0.55\}$. Each test dataset consists of 50 trajectories with the same initial condition. Once the SDE model in Eq. (4) is trained, we simulate it for a long time with the Euler-Maruyama method starting from the same initial condition as the test dataset. We employ Maximum Mean Discrepancy (MMD) [31, 32] to quantify the discrepancy between the predicted and ground-truth trajectories, which is widely used for comparing probability distributions. We use a mixture of radial basis function (RBF) kernels with varying bandwidths to improve the robustness of MMD. For each time point, we calculate the MMD between the marginal distributions of the predicted trajectories and the ground truth trajectories, and report the results averaged over all 9 test datasets.

From Fig. 2 we can observe that when $\lambda = K = 5$, the predicted trajectories achieve the minimal discrepancy from the ground truth trajectories, which correspond well with our theoretical analysis. In fact, for the stochastic Predator-Prey system, the assumptions in Theorem 1 are exactly satisfied. Therefore, it is expected that the optimal hyperparameter λ is equal to K . In subsequent experiments with more complex microscopic dynamics, the assumptions in Theorem 1 may only hold approximately. Thus, the optimal value of λ may deviate slightly from K . We will treat λ as a tunable hyperparameter and perform a hyperparameter search initialized from K in the following experiments.

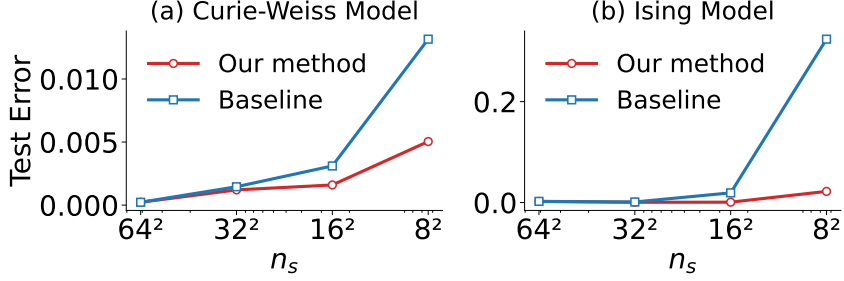


Figure 3: Test error as a function of n_s . The test error is the mean relative error of the mean macroscopic observables between ground-truth and predicted trajectories. (a) Results on the Curie-Weiss model. (b) Results on the Ising model.

3.2 Curie-Weiss model

Having validated our method on a toy SPDE system, we now turn to more complex spin systems. We first consider the Curie-Weiss model, which is a mean-field approximation of the Ising model. The Curie-Weiss model is widely used in statistical mechanics to describe phase transitions due to its simplicity [33, 34]. In this experiment, we conduct an ablation study on the computational power n_s of the microscopic simulator \mathcal{S}_{n_s} , and compare the performance of our method with the baseline across different values of n_s .

The Hamiltonian of the Curie-Weiss Model with n spins is given by:

$$H_{n,h}(\sigma) = -\frac{J}{2n} \sum_{i,j=1}^n \sigma_i \sigma_j - h \sum_{i=1}^n \sigma_i, \quad (19)$$

where $J > 0$ is the interaction strength, h is the external magnetic field and $\sigma_i \in \{-1, 1\}$ denotes the spin state. Throughout the remainder of this paper, we adopt dimensionless units by setting $J = 1$ and the Boltzmann constant $k_B = 1$. Eq. (19) can also be expressed as a function of the magnetization $M = \sum_i \sigma_i/n$:

$$H_{n,h}(\sigma) = -n \left[\frac{J}{2} \left(\frac{\sum_i \sigma_i}{n} \right)^2 + h \frac{\sum_i \sigma_i}{n} \right]. \quad (20)$$

Hence, the microscopic dynamics can be fully characterized by the magnetization. We choose the magnetization as the macroscopic observable of interest since the magnetization is closed by itself, and no additional closure variables are needed.

Strictly speaking, the Curie-Weiss model does not fit directly into our framework, because it is a mean-field model without any explicit spatial structure. To handle this, we imagine the spins are arranged on a square lattice. Moreover, the interaction between spins is nonlocal since each spin interacts with all others through the global coupling. To overcome this, here we take a sufficiently large local patch of size n_s , such that the magnetization computed within the local patch can accurately represent the global magnetization.

In this experiment, the microscopic state is $\mathbf{x} = \{\sigma_1, \dots, \sigma_n\}$. We fix the large-system size $n = 64^2$, while varying the computational power of the microscopic simulator \mathcal{S}_{n_s} by considering $n_s \in \{8^2, 16^2, 32^2, 64^2\}$. When $n_s = 64^2$, our method reduces to the traditional methods for identifying the macroscopic dynamics. The macroscopic observable \mathbf{z}^* is chosen to be the magnetization $\sum_i \sigma_i/n$. No closure variable is needed, and the latent dimension is 1. We consider the microscopic dynamics to be the continuous-time Glauber dynamics [35], as described in Algorithm 2. At each step, the energy differences $\{\Delta H_i\}_{i=1}^n$ and flip rates $\{r_i\}_{i=1}^n$ need to be calculated for all spins.

We generate the small-system distribution \mathcal{D}_s by simulating the continuous-time Glauber dynamics with $h = 0.1$ at temperature $T = 1.1$, which is slightly higher than the critical temperature $T_c = 1$. To generate

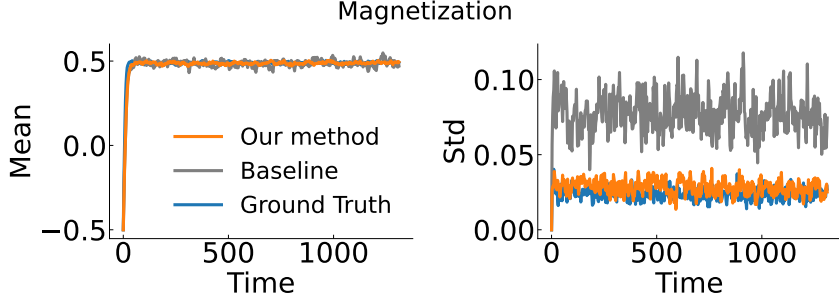


Figure 4: Results on the Curie-Weiss model with $n_s = 16^2$. Mean and standard deviation of the magnetization are estimated from 20 trajectories per method.

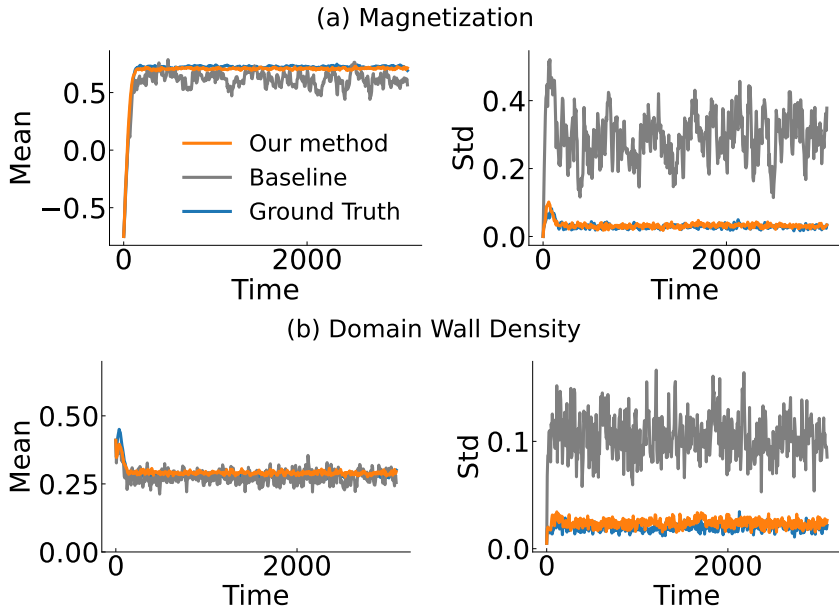


Figure 5: Results on the Ising model with $n_s = 16^2$. Mean and standard deviation are estimated from 20 trajectories per method. (a) Magnetization statistics. (b) Domain wall density statistics.

the large-system data distribution \mathcal{D} , we employ the hierarchical algorithm with $\log_2(n/n_s)$ iterations. For each iteration, we first perform an UPSAMPLE step to replicate every spin into 2^2 block. Next, we perform a LOCALRELAX step by evolving a short-time continuous-time Glauber dynamics locally to remove the unphysical artifacts introduced in the UPSAMPLE step.

Fig. 3 (a) and Fig. 4 compare the performance of our method with the baseline. From Fig. 3 (a), we observe that our method consistently outperforms the baseline when $n_s < n$, which demonstrates the effectiveness of our method. Fig. 4 further compares the magnetization statistics derived from ground truth trajectories with those produced by the baseline model and our method. The statistics of the trajectories predicted by our method align closely with the ground truth, whereas the baseline exhibits much larger variations.

The parameter n_s can influence our method in two ways: (i) The size of the small-system distribution \mathcal{D}_s is n_s . For smaller n_s , more iterations of upsampling are required to obtain \mathcal{D} , which may degrade the data quality of \mathcal{D} . (ii) When generating $\mathbf{x}_{t+\delta t, \mathcal{I}}$ from $\mathbf{x} \sim \mathcal{D}$, we perform partial evolution on a small patch of size n_s . A smaller n_s leads to higher stochasticity of the generated data. As a result, a smaller n_s generally leads to worse performance. The test error of our method remains relatively low when $n_s \geq 16^2$, which demonstrates

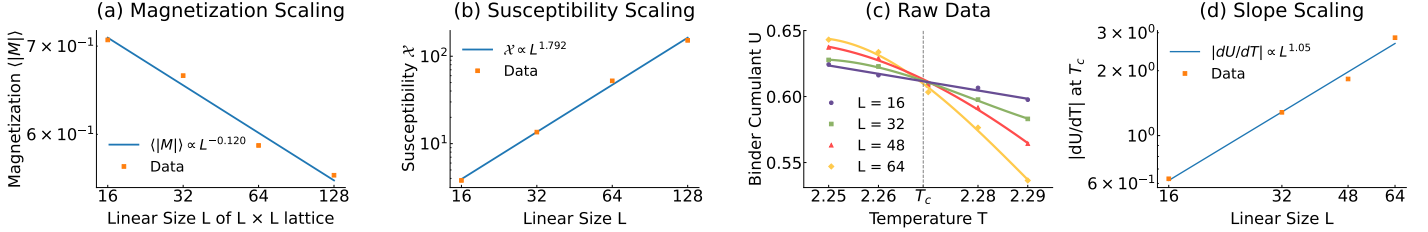


Figure 6: Finite size scaling results of the Ising model at $T = 2.27$, which is very close to $T_c \approx 2.269$. (a) Scaling of the equilibrium magnetization, with a fitted value $(\beta/\nu)^* = 0.120$. (b) Scaling of the magnetic susceptibility, with a fitted value $(\gamma/\nu)^* = 1.792$. (c) Raw Binder cumulant data for different temperatures and linear size L . Linear fitting is used for $L = 16$, and cubic polynomial fitting for $L = 32, 48, 64$. The slope at T_c is extracted from the fitted curve. (d) Log-log plot of $|dU/dT|_{T=T_c}$ versus L , with a fitted value $\nu^* = 1/1.05 \approx 0.95$.

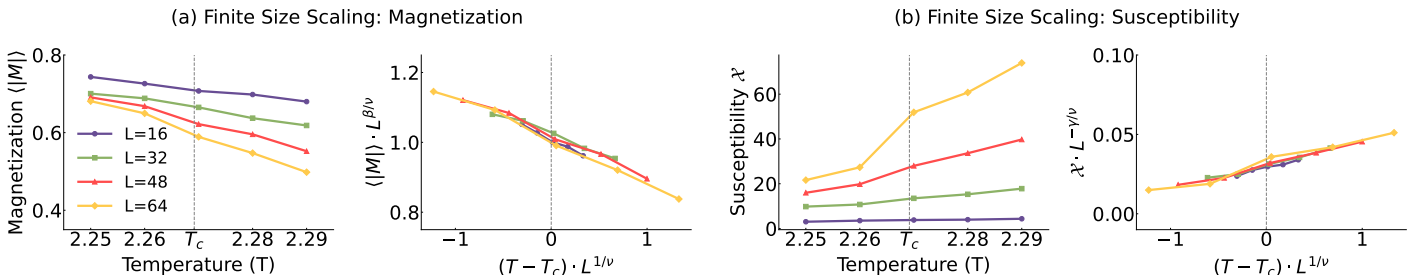


Figure 7: Finite size scaling results of the Ising model across various temperatures and system sizes. The data are collapsed using the theoretical critical exponents. (a) Finite size scaling analysis of the magnetization data calculated from the predicted trajectories by our method. (b) Finite size scaling analysis of the susceptibility.

the robustness of our method *w.r.t.* n_s .

3.3 Ising model

We next validate our method on the Ising model, a more realistic setting than the Curie–Weiss model because it incorporates local interactions and spatial structure. The Ising model plays an important role in statistical physics for investigating order-disorder phase transitions and critical phenomena [36, 37]. We will validate the capability of our method to accurately identify the critical behavior of macroscopic dynamics.

We consider the two-dimensional Ising model, where the spins are arranged on a square lattice of size $n = L \times L$. The Hamiltonian of the Ising model is given by:

$$H_{n,h}(\sigma) = -\frac{J}{2} \sum_{\langle i,j \rangle} \sigma_i \sigma_j - h \sum_{i=1}^n \sigma_i, \quad (21)$$

where $\langle i,j \rangle$ denotes the first nearest neighbor. As in the Curie–Weiss model, we adopt the continuous-time Glauber dynamics as the microscopic dynamics. The critical temperature of the two-dimensional Ising model is $T_c \approx 2.269$. The Ising model exhibits an ordered ferromagnetic phase when $T < T_c$, and a disordered paramagnetic phase when $T > T_c$.

For the macroscopic observables, we consider the magnetization and domain wall density defined by:

$$\rho_{\text{DW}} = \frac{1}{4L^2} \sum_{\langle i,j \rangle} (1 - \sigma_i \sigma_j). \quad (22)$$

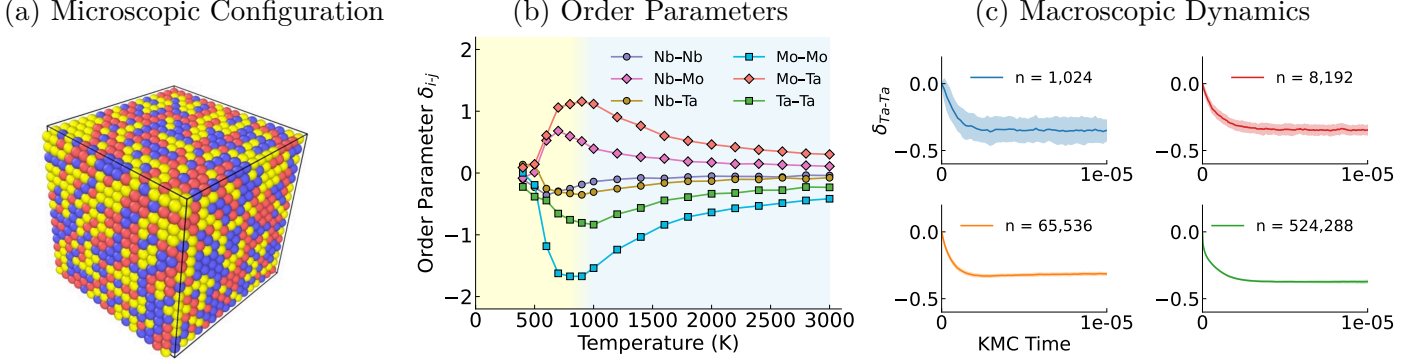


Figure 8: Results of the NbMoTa equimolar alloy system. (a) Microscopic configuration of NbMoTa alloy with 8,192 atoms. (b) Equilibrium order parameters as a function of temperature, obtained from macroscopic dynamics simulations by the trained SDE model. The microscopic system contains $n = 8192$ atoms. (c) Macroscopic dynamics of $\delta_{\text{Ta-Ta}}$ for microscopic systems of varying sizes when $T = 2000K$. The mean and standard deviations are calculated over 100 trajectories.

The domain wall density quantifies the degree of disorder by measuring the proportion of misaligned nearest-neighbor spin pairs. We identify another 2 closure variables by the autoencoder, resulting in a latent state \mathbf{z} of dimension 4.

The experiments are divided into two parts. In the first part, we repeat the procedure of Section 3.2 for the Ising model with $h = 0.1, T = 2.5 > T_c$. We employ the same UPSAMPLE and LOCALRELAX step as used in the Curie-Weiss model for data generation. The results are shown in Fig. 3(b) and Fig. 5. It can be observed that our method achieves lower test error than the baseline. In particular, when $n_s = 8^2$, the test error of the baseline increases significantly, while the test error remains relatively low. Fig. 5 demonstrates that our method can accurately reproduce the statistics of trajectory distributions, while the predicted trajectories of the baseline exhibit much higher variance.

In the second part of the experiment, we demonstrate that our method is capable of capturing the critical behavior of macroscopic dynamics and estimating the critical exponents. Finite-size scaling theory describes how equilibrium observables of a finite system with size $n = L \times L$ scale with L and T near the critical temperature. Specifically, for the equilibrium magnetization $\langle |M| \rangle$ and magnetic susceptibility \mathcal{X} , we will have [38]:

$$\begin{aligned} \langle |M| \rangle(T, L) &= L^{-\beta/\nu} \mathcal{F}_M \left((T - T_c) L^{1/\nu} \right), \\ \mathcal{X}(T, L) &= L^{\gamma/\nu} \mathcal{F}_{\mathcal{X}} \left((T - T_c) L^{1/\nu} \right), \end{aligned} \quad (23)$$

where \mathcal{F}_M and $\mathcal{F}_{\mathcal{X}}$ are scaling functions and the magnetic susceptibility \mathcal{X} is defined as:

$$\mathcal{X} = \frac{L^2}{T} \left(\langle M^2 \rangle - \langle |M|^2 \rangle \right). \quad (24)$$

When $T = T_c$, Eq. (23) simplify to:

$$\begin{aligned} \langle |M| \rangle(T_c, L) &\sim L^{-\beta/\nu}, \\ \mathcal{X}(T_c, L) &\sim L^{\gamma/\nu}. \end{aligned} \quad (25)$$

For the two-dimensional Ising model, the theoretical values of the critical exponents are $\beta = 1/8, \nu = 1, \gamma = 7/4$ [38].

In this part of the experiment, we fix the small-system size to be $n_s = 16^2$, while varying the large-system size $n = L \times L$. We apply our method across different system sizes and a range of temperatures near T_c . Next, we

perform long-time simulations towards equilibrium using the trained SDE models. We calculate the equilibrium magnetization and magnetic susceptibility from the predicted trajectories, to which we fit the critical exponents.

In Fig. 6 (a) and (b), we plot the equilibrium magnetization and susceptibility as a function of L at $T = 2.27$, which is very close to T_c . Next, we fit log-log curves to the data by Eq. (25), yielding estimated critical exponent $(\beta/\nu)^* = 0.120$, $(\gamma/\nu)^* = 1.792$. The estimated critical exponents are very close to the theoretical value $\beta/\nu = 0.125$, $\gamma/\nu = 1.75$. These results show that our method can accurately recover the ratios β/ν and γ/ν , demonstrating its ability to capture accurate macroscopic dynamics across system sizes. This is especially significant because we only use microscopic simulations of small systems with size $n_s = 16^2$, yet our method still succeeds in reproducing macroscopic dynamics for large systems with different sizes.

We further evaluate whether our method can recover the individual critical exponents β, ν, γ . To achieve this, we estimate ν using the Binder cumulant, defined as:

$$U(T, L) = 1 - \frac{\langle M^4 \rangle}{3\langle M^2 \rangle^2}. \quad (26)$$

According to finite-size scaling theory, the slope of the Binder cumulant at the critical temperature will scale with L as follows [38]:

$$|dU/dL|_{T=T_c} \sim L^{1/\nu}. \quad (27)$$

We plot the raw Binder cumulant data in Fig. 6 (c) and compute the slope at T_c by fitting a curve to the data. In Fig. 6 (d), a log-log fit gives the estimated $\nu^* = 0.95$, which is close to the theoretical value of $\nu = 1$.

From Eq. (23), we note that if we plot $\langle |M| \rangle L^{\beta/\nu}$ as a function of $(T - T_c)L^{1/\nu}$, the data should collapse onto the same curve for different T and L . Similarly, $\mathcal{X}L^{-\gamma/\nu}$ and $(T - T_c)L^{1/\nu}$ should also collapse onto the same curve. We present these results in Fig. 7. We can observe that even though the raw magnetization data and raw susceptibility data lie on different curves for different T and L , the scaled data approximately collapse onto the same curve. This validates that our method can accurately capture the critical behavior of macroscopic dynamics in the Ising model.

3.4 NbMoTa alloy

We next validate our method on a more realistic NbMoTa equimolar alloy system to demonstrate its robustness in handling complex microscopic systems. We adopt the experimental setting of Ref. [39], where a neural network was trained to capture energy barriers and used to investigate microscopic diffusion dynamics.

The microscopic diffusion dynamics are modeled using the Kinetic Monte Carlo (KMC) algorithm. In body-centered cubic (BCC) systems such as NbMoTa alloy, each vacancy i can jump to one of its eight first-nearest neighbors with rate $k_{ij} = k_0 \exp(-E_{ij}/k_B T)$, $j = 1, \dots, 8$, where E_{ij} is the energy barrier for the jump to the j -th neighbor and k_0 is an attempt frequency. In our study, we will employ the pretrained neural network model from Ref. [39] for energy barrier calculation. At each KMC step, the transition rates for all vacancies are computed, giving the total jump rate $R_{\text{tot}} = \sum_{i,j} k_{ij}$. Next, the time increment is sampled from the exponential distribution $\Delta t \sim -\frac{\ln r}{R_{\text{tot}}}$, $r \sim \mathcal{U}(0, 1)$. For large systems, the number of vacancies is substantial, and evaluating transition rates for all possible events is computationally demanding.

For the macroscopic observables, we investigate the non-proportional short-range order (SRO) parameters $\delta_{\text{Nb-Nb}}$, $\delta_{\text{Nb-Mo}}$, $\delta_{\text{Nb-Ta}}$, $\delta_{\text{Mo-Mo}}$, $\delta_{\text{Mo-Ta}}$, $\delta_{\text{Ta-Ta}}$. The SRO δ_{ij} is defined by:

$$\delta_{i-j} = \frac{n_{ij} - n_{0,ij}}{n_i}, \quad (28)$$

where n_i is the number of atoms of type i , n_{ij} denotes the number of pairs between atom i and j in the first-nearest neighbor shell, and $n_{0,ij}$ denotes the number of pairs in random solutions. Since we consider an equimolar NbMoTa alloy with BCC structure, $n_{0,ij} = 8/3$. For random configuration, $\delta_{i-j} = 0$. A positive δ_{i-j}

indicates a favored i - j pair, while a negative δ_{i-j} indicates an unfavored i - j pair. The order parameter δ_{i-j} is essentially a rescaled form of the well-studied Warren–Cowley SRO parameter [40–42].

In our experiment, we set the small-system size to $n_s = 1,024$, with a vacancy concentration corresponding to 1 vacancy per 1024 sites. Denote the supercell length by L , then the supercell will consist of $2L^3$ atoms for a BCC lattice. Hence, the supercell length of the small system is $L = 8$. Within the hierarchical upsampling scheme, an UPSAMPLE step is performed by concatenating multiple small-system configurations, followed by a LOCALRELAX step where KMC dynamics are run within small patches to remove unphysical artifacts. We first train an SDE model for the small system with $n_s = 1024$ atoms, and find that learning the macroscopic dynamics of the 6 macroscopic observables directly can already give accurate results consistent with microscopic simulations. Therefore, for the macroscopic dynamics identification of large system from data \mathcal{D} , no closure variables are identified and the latent dimension is 6.

We first consider a large system with $n = 8,192$ atoms. Training data are collected across temperatures from $T = 400K$ to $T = 3000K$, and an SDE model dependent on T is trained:

$$d\mathbf{z}_t = \boldsymbol{\mu}(\mathbf{z}_t, T)dt + \boldsymbol{\Sigma}^{1/2}(\mathbf{z}_t, T)d\mathbf{B}_t. \quad (29)$$

The trained SDE is subsequently simulated for a long time at different temperatures. Fig. 8 (b) shows that the absolute value of $\delta_{\text{Mo-Ta}}$, $\delta_{\text{Ta-Ta}}$, $\delta_{\text{Mo-Mo}}$ increases for $T < 800K$, reach a maximum around $T = 800\sim 900K$, and decrease thereafter. The results indicate a critical temperature around $800 \sim 900K$, corresponding to the regime of maximal diffusion-favored ordering. Our results correspond to the results obtained from the microscopic simulation in Ref. [39], confirming the accuracy and effectiveness of our method in detecting phase transitions.

To assess scalability, we further extend our method to much larger systems with $n = 65,536(L = 32)$ and $n = 524,288(L = 64)$ atoms at $T = 2000K$. In Fig. 8 (c), we show the macroscopic dynamics of $\delta_{\text{Ta-Ta}}$ for different system sizes at $T = 2000K$. While larger systems require more KMC time steps to reach equilibrium, each KMC step corresponds to a smaller time increment. From Fig. 8(c), we observe that the equilibrium KMC time is nearly identical across systems of different sizes. While the mean of the macroscopic dynamics converges approximately to the same value, the trajectories of smaller systems are more stochastic.

4 SUMMARY AND OUTLOOK

This work proposed a framework to learn macroscopic dynamics of large microscopic systems from small-system simulations. We apply our method to SPDEs, spin systems, and an NbMoTa alloy system, scaling it to a large system with 524,288 atoms. Through these applications, we highlight the capability of our model to capture accurate macroscopic dynamics over a wide range of temperatures and system sizes.

Looking ahead, this framework holds significant promise for bridging the gap between microscopic simulations and macroscopic material behavior for complex material systems, such as high-entropy alloys [43–45] and polymer solutions [46, 47]. However, when applied to extremely large systems with billions of atoms, the hierarchical upsampling scheme requires many iterations, and the quality of the generated data distribution \mathcal{D} may deteriorate as the number of iterations increases. We will explore more efficient strategies for generating large-system data distributions \mathcal{D} to mitigate this challenge. By doing so, we envision our framework serving as a powerful tool to accelerate the discovery and design of advanced functional materials for applications in energy storage, catalysis, and structural technologies.

Code Availability

All code used in this work is available at <https://github.com/mengyi-chen/Scalable-learning-of-macroscopic-stochastic-dynamics.git>.

Acknowledgments

This research is supported by the National Research Foundation, Singapore under its AI Singapore Programme (AISG Award No: AISG3-RP-2022-028), the Ministry of Education, Singapore, under its funding for the Research Centre of Excellence Institute for Functional Intelligent Materials (Project No. EDUNC-33-18-279-V12), and Academic Research Fund Tier 3 Grant (Project No. MOET32024-0002).

Appendix

A Continous-time Glauber dynamics

Algorithm 2 Continuous-time Glauber Dynamics

Require:

```

 $\{\sigma_i\}_{i=1}^n$ : Initial spins
 $\beta$ : inverse temperature
 $\text{max\_steps}$ : maximum number of steps
1: Initialize  $\text{step} \leftarrow 0$ ,  $\text{kmc\_time} \leftarrow 0$ 
2: while  $\text{step} < \text{max\_steps}$  do
3:   for  $i = 1$  to  $n$  do
4:     Compute energy differences  $\Delta H_i$  by flipping spin  $i$ 
5:     Compute the rate  $r_i = \frac{1}{1+e^{\beta\Delta H_i}}$ 
6:     Compute the total rate  $R = \sum_{i=1}^N r_i$ 
7:     Sample a spin  $j$  to flip with probability  $r_j/R$ 
8:     Sample time step  $\delta t = -\frac{\ln u}{R}$ ,  $u \sim \mathcal{U}(0, 1)$ 
9:      $\text{kmc\_time} \leftarrow \text{kmc\_time} + \delta t$ ,
10:     $\text{step} \leftarrow \text{step} + 1$ 

```

B Theoretical Analysis

Proof of Theorem 1. The loss function \mathcal{L} and \mathcal{L}_p can be rewritten as:

$$\begin{aligned}\mathcal{L}[\boldsymbol{\mu}, \boldsymbol{\Sigma}] &= \mathbb{E}_{\mathbf{x}_t, \delta t} \mathbb{E}_{\mathbf{x}_{t+\delta t} | \mathbf{x}_t} [-2 \log p(\mathbf{z}_{t+\delta t} | \mathbf{z}_t + \boldsymbol{\mu}(\mathbf{z}_t) \delta t, \boldsymbol{\Sigma}(\mathbf{z}_t) \delta t)], \\ \mathcal{L}_p[\boldsymbol{\mu}, \boldsymbol{\Sigma}] &= \mathbb{E}_{\mathbf{x}_t, \delta t} \mathbb{E}_{\mathcal{I}} \mathbb{E}_{\mathbf{x}_{t+\delta t, \mathcal{I}} | \mathbf{x}_t} [-2 \log p(\mathbf{z}_{t+\delta t, \mathcal{I}} | \mathbf{z}_t + \boldsymbol{\mu}(\mathbf{z}_t) \delta t, K \boldsymbol{\Sigma}(\mathbf{z}_t) \delta t)].\end{aligned}$$

Denote $\mathbf{z}_{t+\delta t} - \mathbf{z}_t - \boldsymbol{\mu}(\mathbf{z}_t) \delta t$ by $\boldsymbol{\delta}(\mathbf{z}_t, \mathbf{z}_{t+\delta t})$ and $\mathbf{z}_{t+\delta t, \mathcal{I}} - \mathbf{z}_t - \boldsymbol{\mu}(\mathbf{z}_t) \delta t$ by $\boldsymbol{\delta}_{\mathcal{I}}(\mathbf{z}_t, \mathbf{z}_{t+\delta t, \mathcal{I}})$. Since p represents the probability distribution of a multivariate normal distribution, we have:

$$\begin{aligned}\mathcal{L}[\boldsymbol{\mu}, \boldsymbol{\Sigma}] &= \mathbb{E}_{\mathbf{x}_t, \delta t} \mathbb{E}_{\mathbf{x}_{t+\delta t} | \mathbf{x}_t} [d \log(2\pi) + \log |\boldsymbol{\Sigma}(\mathbf{z}_t) \delta t| + \boldsymbol{\delta}(\mathbf{z}_t, \mathbf{z}_{t+\delta t})^T (\boldsymbol{\Sigma}(\mathbf{z}_t) \delta t)^{-1} \boldsymbol{\delta}(\mathbf{z}_t, \mathbf{z}_{t+\delta t})], \\ \mathcal{L}_p[\boldsymbol{\mu}, \boldsymbol{\Sigma}] &= \mathbb{E}_{\mathbf{x}_t, \delta t} \mathbb{E}_{\mathcal{I}} \mathbb{E}_{\mathbf{x}_{t+\delta t, \mathcal{I}} | \mathbf{x}_t} [d \log(2\pi) + \log |K \boldsymbol{\Sigma}(\mathbf{z}_t) \delta t| + \boldsymbol{\delta}_{\mathcal{I}}(\mathbf{z}_t, \mathbf{z}_{t+\delta t, \mathcal{I}})^T (K \boldsymbol{\Sigma}(\mathbf{z}_t) \delta t)^{-1} \boldsymbol{\delta}_{\mathcal{I}}(\mathbf{z}_t, \mathbf{z}_{t+\delta t, \mathcal{I}})].\end{aligned}$$

For further simplicity, replace $\boldsymbol{\Sigma}$ by $\boldsymbol{\Lambda} = \boldsymbol{\Sigma}^{-1}$ and omit the dependency of $\boldsymbol{\delta}, \boldsymbol{\delta}_{\mathcal{I}}, \boldsymbol{\mu}, \boldsymbol{\Lambda}$ on $\mathbf{z}_t, \mathbf{z}_{t+\delta t}, \mathbf{z}_{t+\delta t, \mathcal{I}}$, then:

$$\begin{aligned}\hat{\mathcal{L}}[\boldsymbol{\mu}, \boldsymbol{\Lambda}] &= \mathcal{L}[\boldsymbol{\mu}, \boldsymbol{\Sigma}] = \mathbb{E}_{\mathbf{x}_t, \delta t} \mathbb{E}_{\mathbf{x}_{t+\delta t} | \mathbf{x}_t} [d \log(2\pi) + \log(\delta t) - \log |\boldsymbol{\Lambda}| + \frac{1}{\delta t} \boldsymbol{\delta}^T \boldsymbol{\Lambda} \boldsymbol{\delta}], \\ \hat{\mathcal{L}}_p[\boldsymbol{\mu}, \boldsymbol{\Lambda}] &= \mathcal{L}_p[\boldsymbol{\mu}, \boldsymbol{\Sigma}] = \mathbb{E}_{\mathbf{x}_t, \delta t} \mathbb{E}_{\mathcal{I}} \mathbb{E}_{\mathbf{x}_{t+\delta t, \mathcal{I}} | \mathbf{x}_t} [d \log(2\pi) + \log(K \delta t) - \log |\boldsymbol{\Lambda}| + \frac{1}{K \delta t} \boldsymbol{\delta}_{\mathcal{I}}^T \boldsymbol{\Lambda} \boldsymbol{\delta}_{\mathcal{I}}].\end{aligned}$$

We will proceed to calculate the first-order variation and second-order variation of $\hat{\mathcal{L}}$:

$$\begin{aligned}
& \hat{\mathcal{L}}[\boldsymbol{\mu} + \epsilon \mathbf{h}, \boldsymbol{\Lambda} + \epsilon \mathbf{H}] \\
&= \mathbb{E}_{\mathbf{x}_t, \delta t} \mathbb{E}_{\mathbf{x}_{t+\delta t} | \mathbf{x}_t} [d \log(2\pi) + \log(\delta t) - \log |\boldsymbol{\Lambda} + \epsilon \mathbf{H}| + \frac{1}{\delta t} (\boldsymbol{\delta} - \epsilon \mathbf{h} \delta t)^T (\boldsymbol{\Lambda} + \epsilon \mathbf{H}) (\boldsymbol{\delta} - \epsilon \mathbf{h} \delta t)] \\
&= \hat{\mathcal{L}}[\boldsymbol{\mu}, \boldsymbol{\Lambda}] - \mathbb{E}_{\mathbf{x}_t, \delta t} \mathbb{E}_{\mathbf{x}_{t+\delta t} | \mathbf{x}_t} [\log |\boldsymbol{\Lambda} + \epsilon \mathbf{H}| - \log |\boldsymbol{\Lambda}|] \\
&\quad + \epsilon \mathbb{E}_{\mathbf{x}_t, \delta t} \mathbb{E}_{\mathbf{x}_{t+\delta t} | \mathbf{x}_t} [\frac{1}{\delta t} \boldsymbol{\delta}^T \mathbf{H} \boldsymbol{\delta} - 2 \boldsymbol{\delta}^T \boldsymbol{\Lambda} \mathbf{h}] + \frac{\epsilon^2}{2} \mathbb{E}_{\mathbf{x}_t, \delta t} \mathbb{E}_{\mathbf{x}_{t+\delta t} | \mathbf{x}_t} [2 \delta t \mathbf{h}^T \boldsymbol{\Lambda} \mathbf{h} - 4 \boldsymbol{\delta}^T \mathbf{H} \mathbf{h}] + o(\epsilon^2).
\end{aligned}$$

Since

$$\log |\boldsymbol{\Lambda} + \epsilon \mathbf{H}| = \log |\boldsymbol{\Lambda}| + \epsilon \text{tr}(\boldsymbol{\Lambda}^{-1} \mathbf{H}) - \frac{\epsilon^2}{2} \text{tr}(\boldsymbol{\Lambda}^{-1} \mathbf{H} \boldsymbol{\Lambda}^{-1} \mathbf{H}) + o(\epsilon^2),$$

we have:

$$\begin{aligned}
& \hat{\mathcal{L}}[\boldsymbol{\mu} + \epsilon \mathbf{h}, \boldsymbol{\Lambda} + \epsilon \mathbf{H}] \\
&= \hat{\mathcal{L}}[\boldsymbol{\mu}, \boldsymbol{\Lambda}] + \epsilon \mathbb{E}_{\mathbf{x}_t, \delta t} \mathbb{E}_{\mathbf{x}_{t+\delta t} | \mathbf{x}_t} [- \text{tr}(\boldsymbol{\Lambda}^{-1} \mathbf{H}) + \frac{1}{\delta t} \boldsymbol{\delta}^T \mathbf{H} \boldsymbol{\delta} - 2 \boldsymbol{\delta}^T \boldsymbol{\Lambda} \mathbf{h}] \\
&\quad + \frac{\epsilon^2}{2} \mathbb{E}_{\mathbf{x}_t, \delta t} \mathbb{E}_{\mathbf{x}_{t+\delta t} | \mathbf{x}_t} [\text{tr}(\boldsymbol{\Lambda}^{-1} \mathbf{H} \boldsymbol{\Lambda}^{-1} \mathbf{H}) + 2 \delta t \mathbf{h}^T \boldsymbol{\Lambda} \mathbf{h} - 4 \boldsymbol{\delta}^T \mathbf{H} \mathbf{h}] + o(\epsilon^2).
\end{aligned}$$

Hence we have the first variation $\delta \hat{\mathcal{L}}$ and second order variation $\delta^2 \hat{\mathcal{L}}$:

$$\begin{aligned}
\delta \hat{\mathcal{L}} &= \mathbb{E}_{\mathbf{x}_t, \delta t} \mathbb{E}_{\mathbf{x}_{t+\delta t} | \mathbf{x}_t} [- \text{tr}(\boldsymbol{\Lambda}^{-1} \mathbf{H}) + \frac{1}{\delta t} \boldsymbol{\delta}^T \mathbf{H} \boldsymbol{\delta} - 2 \boldsymbol{\delta}^T \boldsymbol{\Lambda} \mathbf{h}], \\
\delta^2 \hat{\mathcal{L}} &= \mathbb{E}_{\mathbf{x}_t, \delta t} \mathbb{E}_{\mathbf{x}_{t+\delta t} | \mathbf{x}_t} [\text{tr}(\boldsymbol{\Lambda}^{-1} \mathbf{H} \boldsymbol{\Lambda}^{-1} \mathbf{H}) + 2 \delta t \mathbf{h}^T \boldsymbol{\Lambda} \mathbf{h} - 4 \boldsymbol{\delta}^T \mathbf{H} \mathbf{h}].
\end{aligned}$$

If $\boldsymbol{\mu}^*, \boldsymbol{\Lambda}^*$ are the minimizer of $\hat{\mathcal{L}}$, we must have $\delta \hat{\mathcal{L}} = 0$ for all the admissible \mathbf{h} and \mathbf{H} . Since

$$\begin{aligned}
\delta \hat{\mathcal{L}} &= \mathbb{E}_{\mathbf{x}_t, \delta t} \mathbb{E}_{\mathbf{x}_{t+\delta t} | \mathbf{x}_t} [- \text{tr}(\boldsymbol{\Lambda}^{-1} \mathbf{H}) + \frac{1}{\delta t} \boldsymbol{\delta}^T \mathbf{H} \boldsymbol{\delta} - 2 \boldsymbol{\delta}^T \boldsymbol{\Lambda} \mathbf{h}] \\
&= \mathbb{E}_{\mathbf{x}_t, \delta t} [\text{tr}(\mathbb{E}_{\mathbf{x}_{t+\delta t} | \mathbf{x}_t} [\frac{1}{\delta t} \boldsymbol{\delta} \boldsymbol{\delta}^T - \boldsymbol{\Lambda}^{-1}] \mathbf{H})] + \mathbb{E}_{\mathbf{x}_t, \delta t} [\mathbb{E}_{\mathbf{x}_{t+\delta t} | \mathbf{x}_t} [-2 \boldsymbol{\delta}^T \boldsymbol{\Lambda}] \mathbf{h}],
\end{aligned}$$

we have:

$$\begin{aligned}
\mathbb{E}_{\mathbf{x}_{t+\delta t} | \mathbf{x}_t} [\frac{1}{\delta t} \boldsymbol{\delta} \boldsymbol{\delta}^T - (\boldsymbol{\Lambda}^*)^{-1}] &= 0 \quad a.e., \\
\mathbb{E}_{\mathbf{x}_{t+\delta t} | \mathbf{x}_t} [-2 \boldsymbol{\delta}^T \boldsymbol{\Lambda}] &= \mathbb{E}_{\mathbf{x}_{t+\delta t} | \mathbf{x}_t} [-2(\mathbf{z}_{t+\delta t} - \mathbf{z}_t - \boldsymbol{\mu}^*(\mathbf{z}_t) \delta t)^T] \boldsymbol{\Lambda}^* (\mathbf{z}_t) = 0 \quad a.e.,
\end{aligned}$$

hence

$$\begin{aligned}
\boldsymbol{\mu}^*(\mathbf{z}_t) &= \frac{1}{\delta t} \mathbb{E}_{\mathbf{x}_{t+\delta t} | \mathbf{x}_t} [\mathbf{z}_{t+\delta t} - \mathbf{z}_t] \quad a.e., \\
\boldsymbol{\Sigma}^*(\mathbf{z}_t) &= (\boldsymbol{\Lambda}^*)^{-1}(\mathbf{z}_t) = \frac{1}{\delta t} \mathbb{E}_{\mathbf{x}_{t+\delta t} | \mathbf{x}_t} [\boldsymbol{\delta} \boldsymbol{\delta}^T] \quad a.e..
\end{aligned}$$

We can calculate the second variation at $\boldsymbol{\mu}^*, \boldsymbol{\Lambda}^*$:

$$\begin{aligned}
\delta^2 \hat{\mathcal{L}} &= \mathbb{E}_{\mathbf{x}_t, \delta t} \mathbb{E}_{\mathbf{x}_{t+\delta t} | \mathbf{x}_t} [\text{tr}(\boldsymbol{\Lambda}^{-1} \mathbf{H} \boldsymbol{\Lambda}^{-1} \mathbf{H}) + 2 \delta t \mathbf{h}^T \boldsymbol{\Lambda} \mathbf{h}] - 4 \mathbb{E}_{\mathbf{x}_t, \delta t} [\mathbb{E}_{\mathbf{x}_{t+\delta t} | \mathbf{x}_t} [(\mathbf{z}_{t+\delta t} - \mathbf{z}_t - \boldsymbol{\mu}^*(\mathbf{z}_t) \delta t)^T] \mathbf{H} \mathbf{h}] \\
&= \mathbb{E}_{\mathbf{x}_t, \delta t} \mathbb{E}_{\mathbf{x}_{t+\delta t} | \mathbf{x}_t} [\text{tr}(\boldsymbol{\Lambda}^{-1} \mathbf{H} \boldsymbol{\Lambda}^{-1} \mathbf{H}) + 2 \delta t \mathbf{h}^T \boldsymbol{\Lambda} \mathbf{h}],
\end{aligned}$$

$\delta^2 \hat{\mathcal{L}} > 0$ if either \mathbf{H} or \mathbf{h} is not equal to zero almost everywhere. Then $\boldsymbol{\mu}^*$ and $\boldsymbol{\Lambda}^*$ are the unique minimizer of functional $\hat{\mathcal{L}}$. Equivalently, $\boldsymbol{\mu}^*$ and $\boldsymbol{\Sigma}^*$ are the unique minimizer of \mathcal{L} . Similarly, we can compute the first-order variation and second-order variation of $\hat{\mathcal{L}}_p$:

$$\hat{\mathcal{L}}_p[\boldsymbol{\mu} + \epsilon \mathbf{h}, \boldsymbol{\Lambda} + \epsilon \mathbf{H}] = \hat{\mathcal{L}}_p[\boldsymbol{\mu}, \boldsymbol{\Lambda}] + \epsilon \delta \hat{\mathcal{L}}_p + \frac{\epsilon^2}{2} \delta^2 \hat{\mathcal{L}}_p + o(\epsilon^2),$$

where

$$\begin{aligned}\delta \hat{\mathcal{L}}_p &= \mathbb{E}_{\mathbf{x}_t, \delta t} \mathbb{E}_{\mathcal{I}} \mathbb{E}_{\mathbf{x}_{t+\delta t, \mathcal{I}} | \mathbf{x}_t} [-\text{tr}(\boldsymbol{\Lambda}^{-1} \mathbf{H}) + \frac{1}{K \delta t} \boldsymbol{\delta}_{\mathcal{I}}^T \mathbf{H} \boldsymbol{\delta}_{\mathcal{I}} - \frac{2}{K} \boldsymbol{\delta}_{\mathcal{I}}^T \boldsymbol{\Lambda} \mathbf{h}], \\ \delta^2 \hat{\mathcal{L}}_p &= \mathbb{E}_{\mathbf{x}_t, \delta t} \mathbb{E}_{\mathcal{I}} \mathbb{E}_{\mathbf{x}_{t+\delta t, \mathcal{I}} | \mathbf{x}_t} [\text{tr}(\boldsymbol{\Lambda}^{-1} \mathbf{H} \boldsymbol{\Lambda}^{-1} \mathbf{H}) + \frac{2 \delta t}{K} \mathbf{h}^T \boldsymbol{\Lambda} \mathbf{h} - \frac{4}{K} \boldsymbol{\delta}_{\mathcal{I}}^T \mathbf{H} \mathbf{h}].\end{aligned}$$

If $\boldsymbol{\mu}^\dagger, \boldsymbol{\Lambda}^\dagger$ are the minimizer of $\hat{\mathcal{L}}_p$, we must have $\delta \hat{\mathcal{L}}_p = 0$ for all the admissible \mathbf{h} and \mathbf{H} . Since

$$\begin{aligned}\delta \hat{\mathcal{L}}_p &= \mathbb{E}_{\mathbf{x}_t, \delta t} \mathbb{E}_{\mathcal{I}} \mathbb{E}_{\mathbf{x}_{t+\delta t, \mathcal{I}} | \mathbf{x}_t} [-\text{tr}(\boldsymbol{\Lambda}^{-1} \mathbf{H}) + \frac{1}{K \delta t} \boldsymbol{\delta}_{\mathcal{I}}^T \mathbf{H} \boldsymbol{\delta}_{\mathcal{I}} - \frac{2}{K} \boldsymbol{\delta}_{\mathcal{I}}^T \boldsymbol{\Lambda} \mathbf{h}] \\ &= \mathbb{E}_{\mathbf{x}_t, \delta t} \left[\text{tr}(\mathbb{E}_{\mathcal{I}} \mathbb{E}_{\mathbf{x}_{t+\delta t, \mathcal{I}} | \mathbf{x}_t} [\frac{1}{K \delta t} \boldsymbol{\delta}_{\mathcal{I}} \boldsymbol{\delta}_{\mathcal{I}}^T - \boldsymbol{\Lambda}^{-1}] \mathbf{H}) \right] + \mathbb{E}_{\mathbf{x}_t, \delta t} \left[\mathbb{E}_{\mathcal{I}} \mathbb{E}_{\mathbf{x}_{t+\delta t, \mathcal{I}} | \mathbf{x}_t} [-\frac{2}{K} \boldsymbol{\delta}_{\mathcal{I}}^T \boldsymbol{\Lambda}] \mathbf{h} \right],\end{aligned}$$

we have

$$\begin{aligned}\mathbb{E}_{\mathcal{I}} \mathbb{E}_{\mathbf{x}_{t+\delta t, \mathcal{I}} | \mathbf{x}_t} [-\frac{2}{K} \boldsymbol{\delta}_{\mathcal{I}}^T \boldsymbol{\Lambda}^\dagger] &= \mathbb{E}_{\mathcal{I}} \mathbb{E}_{\mathbf{x}_{t+\delta t, \mathcal{I}} | \mathbf{x}_t} [-\frac{2}{K} (\mathbf{z}_{t+\delta t, \mathcal{I}} - \mathbf{z}_t - \boldsymbol{\mu}^\dagger(\mathbf{z}_t) \delta t)^T] \boldsymbol{\Lambda}^\dagger(\mathbf{z}_t) = 0 \quad a.e. \\ \mathbb{E}_{\mathcal{I}} \mathbb{E}_{\mathbf{x}_{t+\delta t, \mathcal{I}} | \mathbf{x}_t} [\frac{1}{K \delta t} \boldsymbol{\delta}_{\mathcal{I}} \boldsymbol{\delta}_{\mathcal{I}}^T - (\boldsymbol{\Lambda}^\dagger)^{-1}] &= 0 \quad a.e..\end{aligned}$$

hence

$$\begin{aligned}\boldsymbol{\mu}^\dagger(\mathbf{z}_t) &= \frac{1}{\delta t} \mathbb{E}_{\mathcal{I}} \mathbb{E}_{\mathbf{x}_{t+\delta t, \mathcal{I}} | \mathbf{x}_t} [\mathbf{z}_{t+\delta t, \mathcal{I}} - \mathbf{z}_t] \quad a.e., \\ \boldsymbol{\Sigma}^\dagger(\mathbf{z}_t) &= (\boldsymbol{\Lambda}^\dagger)^{-1}(\mathbf{z}_t) = \frac{1}{K \delta t} \mathbb{E}_{\mathcal{I}} \mathbb{E}_{\mathbf{x}_{t+\delta t, \mathcal{I}} | \mathbf{x}_t} [\boldsymbol{\delta}_{\mathcal{I}} \boldsymbol{\delta}_{\mathcal{I}}^T] \quad a.e..\end{aligned}$$

We can calculate the second variation at $\boldsymbol{\mu}^\dagger, \boldsymbol{\Lambda}^\dagger$:

$$\begin{aligned}\delta^2 \hat{\mathcal{L}}_p &= \mathbb{E}_{\mathbf{x}_t, \delta t} \mathbb{E}_{\mathcal{I}} \mathbb{E}_{\mathbf{x}_{t+\delta t, \mathcal{I}} | \mathbf{x}_t} [\text{tr}(\boldsymbol{\Lambda}^{-1} \mathbf{H} \boldsymbol{\Lambda}^{-1} \mathbf{H}) + \frac{2 \delta t}{K} \mathbf{h}^T \boldsymbol{\Lambda}^\dagger \mathbf{h}] - \frac{4}{K} \mathbb{E}_{\mathbf{x}_t, \delta t} \mathbb{E}_{\mathcal{I}} \mathbb{E}_{\mathbf{x}_{t+\delta t, \mathcal{I}} | \mathbf{x}_t} [\boldsymbol{\delta}_{\mathcal{I}}^T \mathbf{H} \mathbf{h}] \\ &= \mathbb{E}_{\mathbf{x}_t, \delta t} \mathbb{E}_{\mathcal{I}} \mathbb{E}_{\mathbf{x}_{t+\delta t, \mathcal{I}} | \mathbf{x}_t} [\text{tr}(\boldsymbol{\Lambda}^{-1} \mathbf{H} \boldsymbol{\Lambda}^{-1} \mathbf{H}) + \frac{2 \delta t}{K} \mathbf{h}^T \boldsymbol{\Lambda}^\dagger \mathbf{h}],\end{aligned}$$

$\delta^2 \hat{\mathcal{L}}_p > 0$ if either \mathbf{H} or \mathbf{h} is not equal to zero almost everywhere. Then $\boldsymbol{\mu}^\dagger$ and $\boldsymbol{\Lambda}^\dagger$ is the unique minimizer of functional $\hat{\mathcal{L}}$. Equivalently, $\boldsymbol{\mu}^\dagger$ and $\boldsymbol{\Sigma}^\dagger$ are the unique minimizer of \mathcal{L}_p .

Next we will prove $\boldsymbol{\mu}^* = \boldsymbol{\mu}^\dagger, \boldsymbol{\Sigma}^* = \boldsymbol{\Sigma}^\dagger$:

$$\begin{aligned}\boldsymbol{\mu}^*(\mathbf{z}_t) &= \frac{1}{\delta t} \mathbb{E}_{\mathbf{x}_{t+\delta t} | \mathbf{x}_t} [\mathbf{z}_{t+\delta t} - \mathbf{z}_t] \\ &= \frac{1}{K \delta t} \sum_{\mathcal{I}} \mathbb{E}_{\mathbf{x}_{t+\delta t} | \mathbf{x}_t} [\mathbf{z}_{t+\delta t, \mathcal{I}} - \mathbf{z}_t] \\ &= \frac{1}{K \delta t} \sum_{\mathcal{I}} \mathbb{E}_{\tilde{\mathbf{x}}_{t+\delta t, \mathcal{I}} | \mathbf{x}_t} [\mathbf{z}_{t+\delta t, \mathcal{I}} - \mathbf{z}_t].\end{aligned}$$

Since $\mathbf{x}_{t+\delta t, \mathcal{I}} \stackrel{d}{=} \tilde{\mathbf{x}}_{t+\delta t, \mathcal{I}}, \forall I \in \mathcal{I}$,

$$\begin{aligned}\boldsymbol{\mu}^*(\mathbf{z}_t) &= \frac{1}{K \delta t} \sum_{\mathcal{I}} \mathbb{E}_{\mathbf{x}_{t+\delta t, \mathcal{I}} | \mathbf{x}_t} [\mathbf{z}_{t+\delta t, \mathcal{I}} - \mathbf{z}_t] \\ &= \frac{1}{\delta t} \mathbb{E}_{\mathcal{I}} \mathbb{E}_{\mathbf{x}_{t+\delta t, \mathcal{I}} | \mathbf{x}_t} [\mathbf{z}_{t+\delta t, \mathcal{I}} - \mathbf{z}_t] = \boldsymbol{\mu}^\dagger(\mathbf{z}_t), \\ \boldsymbol{\Sigma}^*(\mathbf{z}_t) &= \frac{1}{\delta t} \mathbb{E}_{\mathbf{x}_{t+\delta t} | \mathbf{x}_t} [\boldsymbol{\delta} \boldsymbol{\delta}^T] = \frac{1}{\delta t} \mathbb{E}_{\mathbf{x}_{t+\delta t} | \mathbf{x}_t} [\frac{1}{K^2} \sum_{\mathcal{I}, \mathcal{J}} \boldsymbol{\delta}_{\mathcal{I}} \boldsymbol{\delta}_{\mathcal{J}}^T] \\ &= \frac{1}{K^2 \delta t} \mathbb{E}_{\mathbf{x}_{t+\delta t} | \mathbf{x}_t} [\sum_{\mathcal{I} \neq \mathcal{J}} \boldsymbol{\delta}_{\mathcal{I}} \boldsymbol{\delta}_{\mathcal{J}}^T] + \frac{1}{K^2 \delta t} \mathbb{E}_{\mathbf{x}_{t+\delta t} | \mathbf{x}_t} [\sum_{\mathcal{I}} \boldsymbol{\delta}_{\mathcal{I}} \boldsymbol{\delta}_{\mathcal{I}}^T].\end{aligned}$$

Since $\mathbf{z}_{t+\delta t, \mathcal{I}} - \mathbf{z}_t$ is independent of $\mathbf{z}_{t+\delta t, \mathcal{J}} - \mathbf{z}_t$ when $\mathcal{I} \neq \mathcal{J}$, we have $\mathbb{E}_{\mathbf{x}_{t+\delta t} | \mathbf{x}_t} [\boldsymbol{\delta}_{\mathcal{I}} \boldsymbol{\delta}_{\mathcal{J}}^T]$ when $\mathcal{I} \neq \mathcal{J}$. Then:

$$\boldsymbol{\Sigma}^*(\mathbf{z}_t) = \frac{1}{K^2 \delta t} \mathbb{E}_{\mathbf{x}_{t+\delta t} | \mathbf{x}_t} [\sum_{\mathcal{I}} \boldsymbol{\delta}_{\mathcal{I}} \boldsymbol{\delta}_{\mathcal{I}}^T] = \boldsymbol{\Sigma}^\dagger(\mathbf{z}_t).$$

□

References

- [1] Jose Ordóñez-Miranda, Younès Ezzahri, Karl Joulain, Jérémie Drevillon, and JJ Alvarado-Gil. Modeling of the electrical conductivity, thermal conductivity, and specific heat capacity of vo 2. *Physical Review B*, 98(7):075144, 2018.
- [2] Jacob D Durrant and J Andrew McCammon. Molecular dynamics simulations and drug discovery. *BMC biology*, 9(1):71, 2011.
- [3] Scott A Hollingsworth and Ron O Dror. Molecular dynamics simulation for all. *Neuron*, 99(6):1129–1143, 2018.
- [4] Martin O Steinhauser and Stefan Hiermaier. A review of computational methods in materials science: examples from shock-wave and polymer physics. *International journal of molecular sciences*, 10(12):5135–5216, 2009.
- [5] Deborah K Watson and Martin Dunn. Rearranging the exponential wall for large n-body systems. *Physical review letters*, 105(2):020402, 2010.
- [6] Aron J Cohen, Paula Mori-Sánchez, and Weitao Yang. Challenges for density functional theory. *Chemical reviews*, 112(1):289–320, 2012.
- [7] Michail Stamatakis and Dionisios G Vlachos. Unraveling the complexity of catalytic reactions via kinetic monte carlo simulation: current status and frontiers. *Acs Catalysis*, 2(12):2648–2663, 2012.
- [8] Mie Andersen, Chiara Panosetti, and Karsten Reuter. A practical guide to surface kinetic monte carlo simulations. *Frontiers in chemistry*, 7:202, 2019.
- [9] Miguel Pineda and Michail Stamatakis. Kinetic monte carlo simulations for heterogeneous catalysis: Fundamentals, current status, and challenges. *The Journal of Chemical Physics*, 156(12), 2022.
- [10] Kun Li, Honghui Shang, Yunquan Zhang, Shigang Li, and Baodong Wu. Openkmc: A kmc design for hundred-billion-atom simulation using millions of cores on sunway taihulight. In *SC ’19: The International Conference for High Performance Computing, Networking, Storage, and Analysis*, pages 1–16. ACM, 2019. URL <https://dl.acm.org/doi/10.1145/3295500.3356165>.
- [11] Honghui Shang, Xin Chen, Xingyu Gao, Rongfen Lin, and Lifang Wang. Tensorkmc: Kinetic monte carlo simulation of 50 trillion atoms driven by deep learning on a new generation of sunway supercomputer. In *SC ’21: The International Conference for High Performance Computing, Networking, Storage and Analysis*, pages 1–14. ACM, 2021. ISBN 978-1-4503-8442-1. URL <https://dl.acm.org/doi/10.1145/3458817.3476174>.
- [12] Linfeng Zhang, Jiequn Han, Han Wang, Roberto Car, and Weinan E. Deep potential molecular dynamics: a scalable model with the accuracy of quantum mechanics. *Physical review letters*, 120(14):143001, 2018.
- [13] Simon Batzner, Albert Musaelian, Lixin Sun, Mario Geiger, Jonathan P Mailoa, Mordechai Kornbluth, Nicola Molinari, Tess E Smidt, and Boris Kozinsky. E (3)-equivariant graph neural networks for data-efficient and accurate interatomic potentials. *Nature communications*, 13(1):2453, 2022.
- [14] Jörg Behler and Michele Parrinello. Generalized neural-network representation of high-dimensional potential-energy surfaces. *Physical review letters*, 98(14):146401, 2007.

[15] Justin Gilmer, Samuel S Schoenholz, Patrick F Riley, Oriol Vinyals, and George E Dahl. Neural message passing for quantum chemistry. In *International conference on machine learning*, pages 1263–1272. Pmlr, 2017.

[16] Weile Jia, Han Wang, Mohan Chen, Denghui Lu, Lin Lin, Roberto Car, Weinan E, and Linfeng Zhang. Pushing the limit of molecular dynamics with ab initio accuracy to 100 million atoms with machine learning. In *SC20: International conference for high performance computing, networking, storage and analysis*, pages 1–14. IEEE, 2020.

[17] Aleksander E.P. Durumeric, Nicholas E. Charron, Clark Templeton, Félix Musil, and Klara Bonneau. Machine learned coarse-grained protein force-fields: Are we there yet? *Current Opinion in Structural Biology*, 79:102533, 2023. ISSN 0959440X. URL <https://linkinghub.elsevier.com/retrieve/pii/S0959440X23000076>.

[18] Brooke E. Husic, Nicholas E. Charron, Dominik Lemm, Jiang Wang, and Adrià Pérez. Coarse graining molecular dynamics with graph neural networks. *The Journal of Chemical Physics*, 153(19):194101, 2020. ISSN 0021-9606, 1089-7690. URL <https://pubs.aip.org/jcp/article/153/19/194101/199338/Coarse-graining-molecular-dynamics-with-graph>.

[19] Jonas Köhler, Yaoyi Chen, Andreas Krämer, Cecilia Clementi, and Frank Noé. Flow-matching: Efficient coarse-graining of molecular dynamics without forces. *Journal of Chemical Theory and Computation*, 19(3):942–952, 2023. ISSN 1549-9618, 1549-9626. URL <https://pubs.acs.org/doi/10.1021/acs.jctc.3c00016>.

[20] Jiang Wang, Simon Olsson, Christoph Wehmeyer, Adrià Pérez, and Nicholas E. Charron. Machine learning of coarse-grained molecular dynamics force fields. *ACS Central Science*, 5(5):755–767, 2019. ISSN 2374-7943, 2374-7951. URL <https://pubs.acs.org/doi/10.1021/acscentsci.8b00913>.

[21] Linfeng Zhang, Jiequn Han, Han Wang, Roberto Car, and Weinan E. Deepcg: Constructing coarse-grained models via deep neural networks. *The Journal of Chemical Physics*, 149(3):034101, 2018. ISSN 0021-9606, 1089-7690. URL <https://pubs.aip.org/jcp/article/149/3/034101/196969/DeePCG-Constructing-coarse-grained-models-via-deep>.

[22] Xiaoli Chen, Beatrice W. Soh, Zi-En Ooi, Eleonore Vissol-Gaudin, Haijun Yu, Kostya S. Novoselov, Kedar Hippalgaonkar, and Qianxiao Li. Constructing custom thermodynamics using deep learning. *Nature Computational Science*, 4(1):66–85, 2023. ISSN 2662-8457. URL <https://www.nature.com/articles/s43588-023-00581-5>.

[23] Mengyi Chen and Qianxiao Li. Learning macroscopic dynamics from partial microscopic observations. *Advances in Neural Information Processing Systems*, 37:48996–49021, 2024.

[24] Nicolaas Godfried Van Kampen. *Stochastic processes in physics and chemistry*, volume 1. Elsevier, 1992.

[25] Xiang Fu, Tian Xie, Nathan J. Rebello, Bradley Olsen, and Tommi S. Jaakkola. Simulate time-integrated coarse-grained molecular dynamics with multi-scale graph networks. *Transactions on Machine Learning Research*, 2023. ISSN 2835-8856. URL <https://openreview.net/forum?id=y8RZoPjEUI>.

[26] Anudhyan Boral, Zhong Yi Wan, Leonardo Zepeda-Núñez, James Lottes, Qing Wang, Yi-fan Chen, John Anderson, and Fei Sha. Neural ideal large eddy simulation: Modeling turbulence with neural stochastic differential equations. *Advances in neural information processing systems*, 36:69270–69283, 2023.

[27] Haijun Yu, Xinyuan Tian, Weinan E, and Qianxiao Li. Onsagernet: Learning stable and interpretable dynamics using a generalized onsager principle. *Physical Review Fluids*, 6(11):114402, 2021.

[28] Felix Dietrich, Alexei Makeev, George Kevrekidis, Nikolaos Evangelou, and Tom Bertalan. Learning effective stochastic differential equations from microscopic simulations: Linking stochastic numerics to deep learning. *Chaos: An Interdisciplinary Journal of Nonlinear Science*, 33(2):023121, 2023. ISSN 1054-1500, 1089-7682. URL <https://pubs.aip.org/cha/article/33/2/023121/2876122/Learning-effective-stochastic-differential>.

[29] Zhen Zhang, Yeonjong Shin, and George Em Karniadakis. Gfinns: Generic formalism informed neural networks for deterministic and stochastic dynamical systems. *Philosophical Transactions of the Royal Society A*, 380(2229):20210207, 2022.

[30] Ting-Ting Gao, Baruch Barzel, and Gang Yan. Learning interpretable dynamics of stochastic complex systems from experimental data. *Nature Communications*, 15(1):6029, 2024. ISSN 2041-1723. URL <https://www.nature.com/articles/s41467-024-50378-x>.

[31] Arthur Gretton, Karsten M Borgwardt, Malte J Rasch, Bernhard Schölkopf, and Alexander Smola. A kernel two-sample test. *The journal of machine learning research*, 13(1):723–773, 2012.

[32] Patrick Kidger, James Foster, Xuechen Li, and Terry J Lyons. Neural sdes as infinite-dimensional gans. In *International conference on machine learning*, pages 5453–5463. PMLR, 2021.

[33] Martin Kochmański, Tadeusz Paszkiewicz, and Sławomir Wolski. Curie–weiss magnet—a simple model of phase transition. *European Journal of Physics*, 34(6):1555, 2013.

[34] Richard S Ellis. *Entropy, large deviations, and statistical mechanics*, volume 271. Springer Science & Business Media, 2012.

[35] Roy J Glauber. Time-dependent statistics of the ising model. *Journal of mathematical physics*, 4(2):294–307, 1963.

[36] Stephen G Brush. History of the lenz-ising model. *Reviews of modern physics*, 39(4):883, 1967.

[37] Barry A Cipra. An introduction to the ising model. *The American Mathematical Monthly*, 94(10):937–959, 1987.

[38] Anders W Sandvik. Computational studies of quantum spin systems. In *AIP Conference Proceedings*, volume 1297, pages 135–338. American Institute of Physics, 2010.

[39] Bin Xing, Timothy J. Rupert, Xiaoqing Pan, and Penghui Cao. Neural network kinetics for exploring diffusion multiplicity and chemical ordering in compositionally complex materials. *Nature Communications*, 15(1):3879, 2024. ISSN 2041-1723. URL <https://www.nature.com/articles/s41467-024-47927-9>.

[40] JM Cowley. Short-range order and long-range order parameters. *Physical Review*, 138(5A):A1384, 1965.

[41] Antonio Fernández-Caballero, JS Wróbel, PM Mummery, and D Nguyen-Manh. Short-range order in high entropy alloys: theoretical formulation and application to mo-nb-ta-vw system. *Journal of Phase Equilibria and Diffusion*, 38(4):391–403, 2017.

[42] Ying Han, Hangman Chen, Yongwen Sun, Jian Liu, Shaolou Wei, Bijun Xie, Zhiyu Zhang, Yingxin Zhu, Meng Li, Judith Yang, et al. Ubiquitous short-range order in multi-principal element alloys. *Nature Communications*, 15(1):6486, 2024.

[43] Won-Mi Choi, Yong Hee Jo, Seok Su Sohn, Sunghak Lee, and Byeong-Joo Lee. Understanding the physical metallurgy of the cocrfemnni high-entropy alloy: an atomistic simulation study. *npj Computational Materials*, 4(1):1, 2018.

- [44] Tatiana Kostiuchenko, Fritz Körmann, Jörg Neugebauer, and Alexander Shapeev. Impact of lattice relaxations on phase transitions in a high-entropy alloy studied by machine-learning potentials. *npj Computational Materials*, 5(1):55, 2019.
- [45] Yifan Cao, Killian Sheriff, and Rodrigo Freitas. Capturing short-range order in high-entropy alloys with machine learning potentials. *npj Computational Materials*, 11(1):268, 2025.
- [46] Kurt Kremer and Kurt Binder. Monte carlo simulation of lattice models for macromolecules. *Computer Physics Reports*, 7(6):259–310, 1988.
- [47] Thomas E Gartner III and Arthi Jayaraman. Modeling and simulations of polymers: a roadmap. *Macromolecules*, 52(3):755–786, 2019.
- [48] Alberto Ferrari, Fritz Körmann, Mark Asta, and Jörg Neugebauer. Simulating short-range order in compositionally complex materials. *Nature computational science*, 3(3):221–229, 2023.